Article

Voltage and Overpotential Prediction of Vanadium Redox Flow Batteries with Artificial Neural Networks

Joseba Martínez-López [1], Koldo Portal-Porras [1], Unai Fernández-Gamiz [1,*], Eduardo Sánchez-Díez [2], Javier Olarte [2] and Isak Jonsson [3]

[1] Nuclear Engineering and Fluid Mechanics Department, University of the Basque Country UPV/EHU, Nieves Cano 12, 01006 Vitoria-Gasteiz, Spain; joseba.martinezl@ehu.eus (J.M.-L.); koldo.portal@ehu.eus (K.P.-P.)
[2] Centre for Cooperative Research on Alternative Energies (CIC EnergiGUNE), Basque Research and Technology Alliance (BRTA), Alava Technology Park, Albert Einstein 48, 01510 Vitoria-Gasteiz, Spain; esanchez@cicenergigune.com (E.S.-D.); jolarte@cicenergigune.com (J.O.)
[3] Department of Mechanics and Maritime Sciences, Division of Fluid Dynamics, Chalmers University of Technology, SE-41296 Gothenburg, Sweden; isak.jonsson@chalmers.se
* Correspondence: unai.fernandez@ehu.eus

Abstract: This article explores the novel application of a trained artificial neural network (ANN) in the prediction of vanadium redox flow battery behaviour and compares its performance with that of a two-dimensional numerical model. The aim is to evaluate the capability of two ANNs, one for predicting the cell potential and one for the overpotential under various operating conditions. The two-dimensional model, previously validated with experimental data, was used to generate data to train and test the ANNs. The results show that the first ANN precisely predicts the cell voltage under different states of charge and current density conditions in both the charge and discharge modes. The second ANN, which is responsible for the overpotential calculation, can accurately predict the overpotential across the cell domains, with the lowest confidence near high-gradient areas such as the electrode membrane and domain boundaries. Furthermore, the computational time is substantially reduced, making ANNs a suitable option for the fast understanding and optimisation of VRFBs.

Keywords: ANN; vanadium redox flow battery; numerical model; cell potential; two-dimensional; overpotential; states of charge

1. Introduction

Deploying effective and scalable energy storage systems is becoming increasingly important as we move toward carbon-neutral emissions and a sustainable energy future [1,2]. The integration of intermittent renewable energy sources into our energy infrastructure is imperative, considering the commitment to achieve carbon neutrality. The development of large-scale energy storage systems is vital for this integration and maximising the use of renewable resources while maintaining the stability of the electric grid. Redox flow batteries (RFBs) have become one of the front-runners among the several available choices [3–6]. They are distinguished by the separation of the energy storage capacity from the power output, because RFBs store energy in chemical solutions contained in external tanks, allowing the capacity to be scaled independently of the power density [7,8]. This decoupling of energy and power renders RFBs exceptionally flexible for a wide range of applications.

Arguably, vanadium-based redox flow batteries (VRFBs) are the most promising technology for commercial implementation [9,10]. Invented by M. Skyllas-Kazacos et al. [11] in the 1980s, VRFBs employ only one single element, vanadium, in different oxidation states for both electrolytes, thus reducing the cross-contamination risk [12]. Moreover, VRFB systems exhibit noteworthy characteristics in terms of cyclability, energy efficiency, response

time, safe operation, remarkable energy storage capability, and incorporating readily recyclable components to minimize overall costs over the system lifetime [11,13–17]. This sets them apart from other RFB technologies, such as zinc-based chemistries, which present hydrogen evolution in charging, dendrite formation, and uneven metal deposition, which then lead to cell failure [3,18,19]. Organic-based RFBs have gained attention for their use of abundant, non-expensive organic compounds, but they still face challenges arising from cycling stability and reactant decomposition [6,20,21]. A more in-depth investigation is imperative to consolidate this technology for future scalability and commercial implementation.

Figure 1 depicts a visual representation of a single cell from a VRFB. The electrolytes are stored in two separate tanks. The positive electrolyte contains VO_2^+ and VO^{2+} ions, while the negative electrolyte has V^{2+} and V^{3+} ions. Both electrolytes are recirculated by pumps into the cell. The electrodes, inside the cell, provide an active area for the electrochemical redox reactions to occur. To prevent cross-contamination and allow for protons to pass and preserve the charge conservation, an ion-selective membrane is added between both electrodes [22].
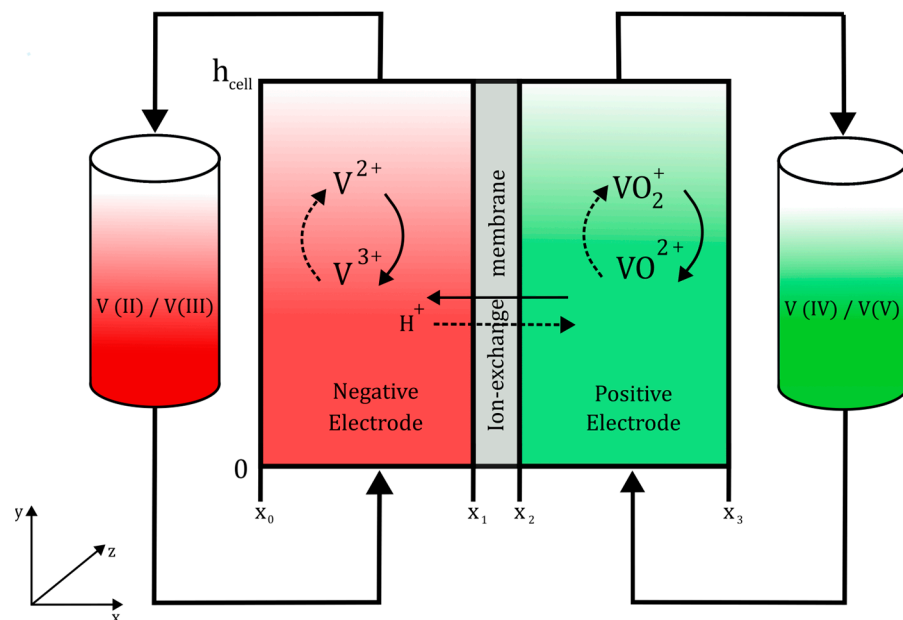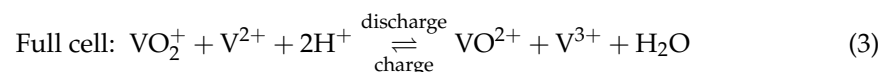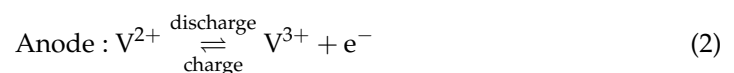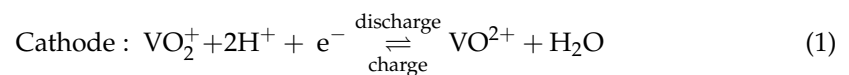

Figure 1. Schematic of the VRFB cell employed, with the negatively charged fluid symbolised in red and the positively charged fluid denoted in green. Additional details can be found in the text.

The chemical reactions occurring in the half-cells and the full cell are as follows:

$$\text{Cathode}: VO_2^+ + 2H^+ + e^- \underset{\text{charge}}{\overset{\text{discharge}}{\rightleftharpoons}} VO^{2+} + H_2O \tag{1}$$

$$\text{Anode}: V^{2+} \underset{\text{charge}}{\overset{\text{discharge}}{\rightleftharpoons}} V^{3+} + e^- \tag{2}$$

$$\text{Full cell}: VO_2^+ + V^{2+} + 2H^+ \underset{\text{charge}}{\overset{\text{discharge}}{\rightleftharpoons}} VO^{2+} + V^{3+} + H_2O \tag{3}$$

The experimental evaluation of VRFB performance is the conventional approach to assess performance, but it has a considerable financial burden. As the use of VRFBs in various applications has become increasingly popular, there is a growing need for cost-effective methods and strategies to understand and optimise their performance and system integration. Numerical models offer a rapid and iterative design approach, allowing researchers to easily modify system parameters, electrode geometries, and operating conditions. This

approach enables the exploration of various design configurations and identification of optimal operating conditions more efficiently than traditional experimental methods.

A wide range of numerical investigations of VRFBs is available in the public literature, ranging from basic zero-dimensional models [23–25] to the most complex three-dimensional models [26–31]. The use of numerical models to simulate flow batteries involves a careful balance between computational cost and accuracy. Zero- and one-dimensional models are particularly helpful for preliminary evaluations, down-selection, and fast exploratory studies, but have the limitation of oversimplifying the complex behaviour of VRFBs, neglecting spatial variations and non-uniformities within the battery cell. The need for computational resources increases significantly as the accuracy of numerical simulations is improved to include aspects such as concentration profiles, potential, and current density distributions [28–31] or capture intricate time-dependent fluid–membrane interactions. However, recent advancements in Artificial Neural Networks (ANNs) have enabled the creation of accurate models trained on data obtained from Computational Fluid Dynamics (CFD) simulations. These surrogate models offer the flexibility and speed of low-fidelity models, while incorporating many aspects of advanced computational models. In the field of fluid mechanics, several studies have used ANNs to model different cases, such as active [32] and passive flow control devices [33], vehicle aerodynamics [34], thermal systems [35], and multiphase-state systems [36], to mention a few.

The primary objective of this study was to model a VRFB using Artificial Neural Networks (ANNs). To accomplish this, numerical simulations were performed to generate training and benchmark data. By altering the current densities and states of charge in these simulations, a comprehensive dataset was created. Specifically, two distinct ANNs were designed and trained: one for predicting the voltage and the other for predicting the overpotential.

2. Materials and Methods

2.1. Governing Equations

The model presented in this work consists of three domains: positive electrode, ion exchange membrane, and negative electrode. The current work utilizes a Nafion type cation exchange membrane. This choice aligns with the conventional approach in the literature and is consistent with the experimental validation. However, newly developed anion exchange membranes show promising results in terms of lower vanadium crossover and cost and enhanced H^+ permeability [37]. The following assumptions were made in the numerical model:

- Stationary conditions;
- Incompressible electrolytes;
- The fluids were assumed to be completely diluted;
- Side reactions were neglected;
- Both electrodes and the membrane were considered isothermal;
- The properties of the electrodes, electrolyte, and membrane were isotropic;
- Changes in the z-direction of the cell were ignored (depth in Figure 1).

The model was based on works published by Shah et al. [38] and Knehr et al. [39]. The conservation of mass of the charged species can be expressed by Equation (4).

$$\frac{\partial}{\partial t}(\varepsilon c_i) + \nabla \cdot \vec{N}_i = -S_i \tag{4}$$

Variable ε refers to the electrode porosity, c_i is the concentration of species i, and S_i is the source term of the species (listed in Table 1).

Table 1. Source terms for species in the positive and negative electrodes.

Source Term	Positive Electrode	Negative Electrode
S_{II} (V(II) mass conservation equation)	-	$\vec{i}/F$
S_{III} (V(III) mass conservation equation)	-	$-\vec{i}/F$
S_{IV} (V(IV) mass conservation equation)	$\vec{i}/F$	-
S_V (V(V) mass conservation equation)	$-\vec{i}/F$	-
S_{H^+} (proton concentration equation)	-	$-2\nabla \cdot \vec{i}/F$

$\vec{N}_i$ is the charged species flux described by the Nernst–Planck equation, as shown in Equation (5).

$$\vec{N}_i = -D_i^{eff}\nabla c_i - z_i u_i c_i F\nabla\varphi_l + \vec{u}c_i \tag{5}$$

The first term accounts for diffusion, where D_i^{eff} is effective diffusivity. In the second term (migration term), z_i represents the charge of species i, u_i is the ionic mobility, F is the Faraday constant, and φ_l is the liquid potential. In the third term (convection), $\vec{u}$ represents electrolyte velocity.

The effective diffusivity, D_i^{eff}, was obtained from the Bruggemann correlation as shown in Equation (6).

$$D_i^{eff} = \varepsilon^{3/2}D_i \tag{6}$$

The ionic mobility u_i was calculated using the Nernst–Einstein equation, as shown in Equation (7), where R is the universal gas constant and T is the temperature.

$$u_i = \frac{D_i^{eff}}{RT} \tag{7}$$

The electrolyte velocity, represented by $\vec{u}$ in Equation (5) in the convection term, is calculated by means of Darcy's Law, as shown in Equation (8), where p is the pressure and μ is the dynamic viscosity of the electrolyte, as indicated in Table 2, among the other electrolyte properties.

$$\vec{u} = -\frac{K}{\mu}\nabla p \tag{8}$$

Table 2. Electrolyte properties.

Term	Symbol	Value
V(II) diffusion coefficient	D_{V2}	2.4×10^{-10} m^{2}s^{-1} [40]
V(III) diffusion coefficient	D_{V3}	2.4×10^{-10} m^{2}s^{-1} [40]
V(IV) diffusion coefficient	D_{V4}	3.9×10^{-10} m^{2}s^{-1} [40]
V(V) diffusion coefficient	D_{V5}	3.9×10^{-10} m^{2}s^{-1} [40]
HSO$_4^-$ diffusion coefficient	$D_{HSO_4^-}$	1.33×10^{-9} m^{2}s^{-1} [41]
SO$_4^{2-}$ diffusion coefficient	$D_{SO_4^{2-}}$	1.065×10^{-9} m^{2}s^{-1} [41]
H$^+$ diffusion coefficient	D_{H^+}	9.312×10^{-9} m^{2}s^{-1} [41]
Dynamic viscosity	μ	4.9238×10^{-3} Pa s [42]

K represents the porous electrode permeability calculated using the Kozeny–Carman equation, as shown in Equation (9), where d_f is the fibre diameter and k_{ck} is the Kozeny–Carman constant.

$$K = \frac{d_f^2\varepsilon^3}{16k_{ck}(1-\varepsilon)^2} \tag{9}$$

To fulfil the condition of electroneutrality, Equation (10) was solved for all charged species, except for $SO_4{}^{2-}$:

$$\sum_i z_i c_i = 0 \tag{10}$$

To integrate the species balance with electrochemical reactions and the current flow within the electrode during the charge/discharge processes, the charge conservation equation was solved, as shown in Equation (11).

$$\nabla \cdot \overrightarrow{i}_l = -\nabla \cdot \overrightarrow{i}_s = \overrightarrow{i}_R \tag{11}$$

Equation (11) indicates that the electrochemical reaction rate (i_R) directly corresponds to the charges leaving the electrolyte $\overrightarrow{i}_l$, which in turn equate to the charges entering the electrode $\overrightarrow{i}_s$. Both the liquid and solid current densities are expressed by Equations (12) and (13).

$$\overrightarrow{i}_l = F\sum_i z_i \overrightarrow{N}_i \tag{12}$$

$$\overrightarrow{i}_s = -\sigma_s^{eff} \nabla \varphi_s \tag{13}$$

The term σ_s^{eff}, which corresponds to the effective conductivity of the porous electrode, was calculated using Equation (14), where σ_s is the electrode bulk conductivity, listed in Table 3, with other parameters related to the electrodes.

$$\sigma_s^{eff} = (1 - \varepsilon)^{\frac{3}{2}} \sigma_s \tag{14}$$

Table 3. Electrode properties.

Term	Symbol	Value
Electronic conductivity	σ_s	1×10^3 S m^{-1} [42]
Porosity	ε	0.929 [43]
Specific surface area	a	1.62×10^4 m^2 [43]
Kozeny–Carman constant	k_{ck}	4.28 [42]
Electrode fibre diameter	d_f	1.76×10^{-5} m [43]

An integration with the Butler–Volmer law, which characterizes the electrochemical reactions occurring at the surface of the porous carbon electrode, is utilised to converge the conservation equations. Following this, the electrochemical reaction rate (i_R) was calculated for both electrodes, positive ("+") and negative ("−"), as shown in Equation (15) and Equation (16), respectively.

$$i_{R+} = ai_{0,+}\left[exp\left(\frac{(1-\alpha_+)F\eta_+}{RT}\right) - exp\left(\frac{-\alpha_+ F\eta_+}{RT}\right)\right] \tag{15}$$

$$i_{R-} = ai_{0,-}\left[exp\left(\frac{(1-\alpha_-)F\eta_+}{RT}\right) - exp\left(\frac{-\alpha_- F\eta_+}{RT}\right)\right] \tag{16}$$

The specific surface area of the electrode was represented by a, α is the charge transfer coefficient, and η denotes the overpotential. $i_{0,+}$ and $i_{0,-}$, the exchange current densities, are expressed as shown in Equations (17) and (18), where k_+ and k_- are the reaction rate constants for the positive and negative side, respectively.

$$i_{0,+} = Fk_+(c_{IV})^{(1-\alpha_+)}(c_V)^{\alpha_+} \tag{17}$$

$$i_{0,-} = Fk_-(c_{II})^{(1-\alpha_-)}(c_{III})^{\alpha_-} \tag{18}$$

Table 4 lists the kinetic parameters used in Equations (17) and (18).

Table 4. Kinetic parameters.

Term	Symbol	Value
Cathodic transfer coefficient	α_+	0.5 [42]
Anodic transfer coefficient	α_-	0.5 [42]
Standard rate constant for positive reaction	k_+	6.8×10^{-7} m s^{-1} [40]
Standard rate constant for negative reaction	k_-	1.7×10^{-7} m s^{-1} [44]
Standard equilibrium potential for positive side	E'_+	1.004 V [38]
Standard equilibrium potential for negative side	E'_-	-0.255 V [38]

The overpotential was determined for the positive and negative reactions using Equations (19) and (20).

$$\eta_+ = \varphi_s - \varphi_l - E_+ \tag{19}$$

$$\eta_- = \varphi_s - \varphi_l - E_- \tag{20}$$

The standard equilibrium potentials E_+ and E_- were obtained using the Nernst equation, as shown in Equations (21) and (22).

$$E_+ = E'_+ + \frac{RT}{F} ln\left(\frac{c_{III}}{c_{II}}\right) \tag{21}$$

$$E_- = E'_- + \frac{RT}{F} ln\left(\frac{c_V \cdot (c_{H+})^2}{c_{IV}}\right) \tag{22}$$

The effective conductivity of the membrane σ_m^{eff} can be modelled as shown in Equation (23), where $D_{H^+}^{eff}$ denotes the proton effective diffusion coefficient.

$$\sigma_m^{eff} = \frac{F^2}{RT} z_i^2 D_{H^+}^{eff} c_{H^+} \tag{23}$$

2.2. Boundary Conditions

Figure 1 x and y coordinates were taken as references for the boundary condition description. At $x = x_0$, the anode external boundary is set as an electrical ground, that is, the solid potential is equal to zero:

$$\varphi_s = 0 \quad x = x_0 \tag{24}$$

The species fluxes at the top and bottom of the membrane and the external boundaries of the electrodes are zero, aside from the inlets and outlets:

$$-\vec{n} \cdot \vec{N_i} = 0 \begin{cases} x = x_0 \text{ and } x = x_3 \\ x = x_1 \text{ and } x = x_2 \text{ (except protons)} \\ y = 0 \text{ and } y = h_e \end{cases} \tag{25}$$

At $y = 0$, a boundary was set for the flux entering the cell through the electrodes.

$$\left.\begin{array}{l} c_i = c_i^{in} \\ \vec{n} \cdot \vec{u} = \frac{Q}{\varepsilon w_e L_e} \end{array}\right\} \begin{array}{c} x_0 < x < x_1 \text{ and } x_2 < x < x_3 \\ y = 0 \end{array} \tag{26}$$

where Q is the volumetric flow rate, w_{cell} is the cell width, and L_e is the electrode thickness. Analogously, the electrodes have a pressure outlet at $y = h_{cell}$, and the flux of the species caused by diffusion is neglected.

$$\left.\begin{array}{l} p = p_{out} \\ -D_i^{eff} \nabla c_i \cdot \vec{n} = 0 \end{array}\right\} \begin{array}{c} x_0 < x < x_1 \text{ and } x_2 < x < x_3 \\ y = h_e \end{array} \tag{27}$$

A constant current density was applied to the external boundary of the cathode using Equation (28).

$$-\vec{n} \cdot \vec{i}_s = i_{avg} \quad x = x_3 \tag{28}$$

where i_{avg} denotes the user-defined current applied to the boundary. The sign of this parameter determines whether the cell is in charge or discharge. This leads to the application of an electrical insulation to the upper and lower boundaries of the membranes and electrodes.

$$\left. \begin{array}{l} -\vec{n} \cdot \vec{i}_s = 0 \\ -\vec{n} \cdot \vec{i}_l = 0 \end{array} \right\} \quad \begin{array}{l} x_0 < x < x_3 \\ y = 0 \text{ and } y = h_e \end{array} \tag{29}$$

The geometrical dimensions and operating conditions of the cell are listed in Table 5.

Table 5. Operating conditions and cell geometrical parameters.

Term	Symbol	Value
Temperature	T	298 K
State of Charge	SOC	50%
Volumetric flow rate	Q	60 mL min^{-1}
Outlet pressure	p_{out}	0 Pa
Electrode thickness	L_e	0.003 m [42]
Electrode width	w_e	0.025 m [42]
Electrode length	h_e	0.02 m [42]
Membrane thickness	L_m	125 μm [42]

2.3. Numerical Model

The cell was modelled using the commercial software COMSOL Multiphysics 5.5 with its incorporated physics packages, including Darcy's law and tertiary current distribution. By employing the finite element method, the model featured a structured mesh made of 4616 quadratic elements. The computational approach adhered to a relative error set at 1.0×10^{-6}.

2.4. Neural Network

In the present study, a multilayer perceptron with backpropagation (MLP-BP) is used, which is a multilayer model with hidden layers. In this model, the output y is estimated using Equation (30). The output of each hidden neuron is calculated with the sigmoid function defined in Equation (31), which receives as input the postsynaptical h_i of each i neuron from the previous layer, calculated with the linear combination defined in Equation (32), where x represents the inputs to the layers, ω the weights of the layers, and θ the biases.

$$y = \sum_{i=1}^{i=N_{hidden}} \omega_i \cdot g_i\left(\vec{x}\right) + \theta \tag{30}$$

$$g_i\left(\vec{x}\right) = \frac{1}{1 + e^{-h_i}} \tag{31}$$

$$h_i\left(\vec{x}\right) = \sum_{j=1}^{j=N_{hidden}} \omega'_{i,j} \cdot x_j + \theta'_i \tag{32}$$

The commercial software MATLAB 2022a [45], commercial code with its Deep Learning toolbox [46], was used to design and train the ANN.

The number of hidden layers and neurones in each network depended on the complexity of the magnitude considered. Hence, two different networks were trained for the two targeted ANN models: one for voltage prediction, as shown in Figure 2, and the other for overpotential prediction, as shown in Figure 3. The training data were split into 70% training, 20% validation, and 10% testing for both networks.
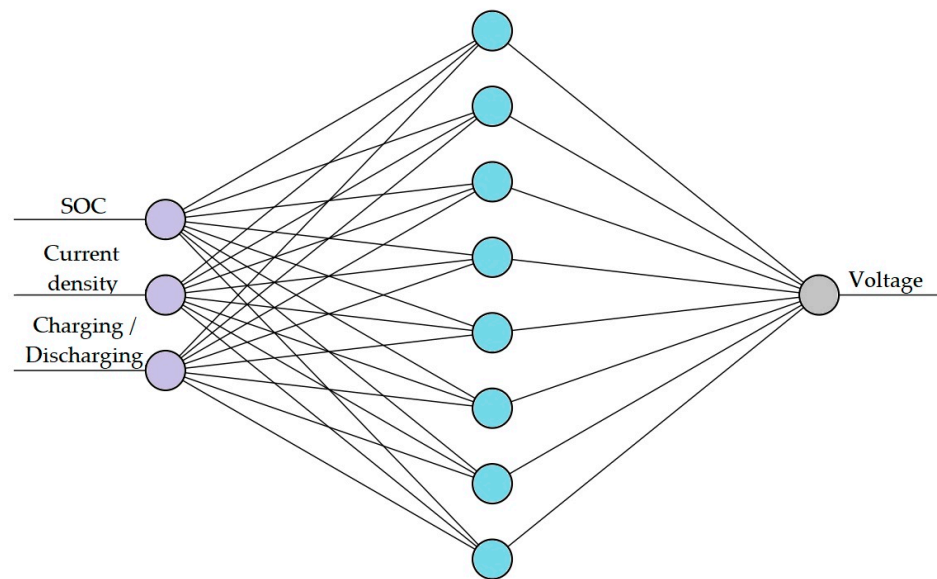
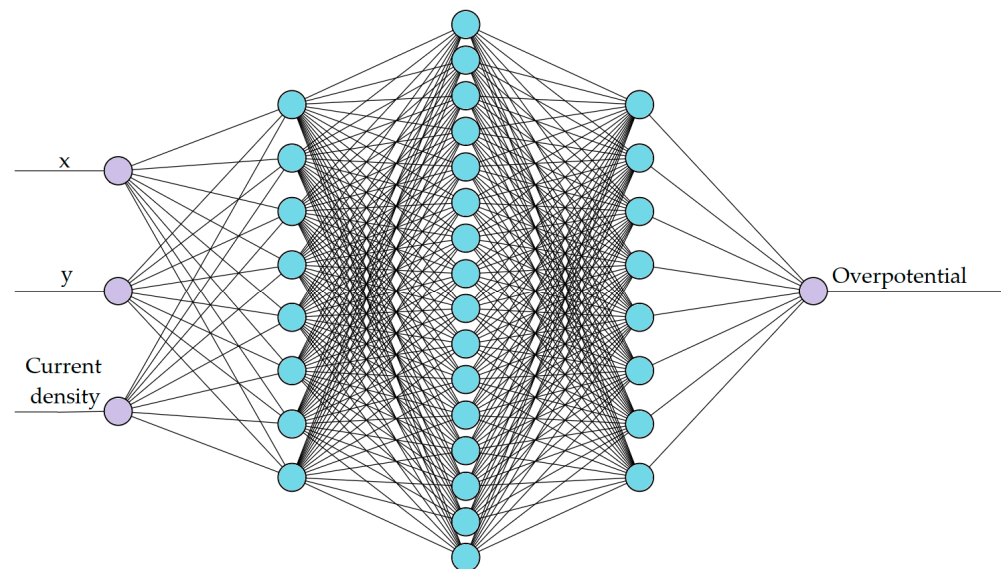**Figure 2.** Architecture of the ANN for voltage prediction.

Figure 3. Architecture of the ANN for overpotential prediction.

The first network (ANN1) predicts the voltage of the cell under charge and discharge regimes for different charge and current densities. ANN1 is a relatively simple ANN with a single input layer comprising three parameters: SoC, Current density, Charging or Discharging, a single hidden layer with eight nodes, and an output layer with a single node. Figure 2 shows the architecture of ANN1.

The second network (ANN2) aims to predict the spatial overpotential of the cell for a constant State of Charge of 50% which is expected to be substantially less continuous compared to ANN1. Hence, added complexity is required in ANN2 which contains three hidden layers (with 8, 16, and 8 nodes) and an output layer with a single node for the overpotential. Figure 3 shows the architecture of the ANN2.

The ANNs are benchmarked using the standard Pearson product-moment correlation coefficient R.

3. Results

3.1. Model Validation

The numerical model was validated using experimental data from You et al. [28], which involved placing a 5 cm^2 cell in a static solution and measuring the charge-discharge curves at two different current densities: 40 mA cm^{-2} and 80 mA cm^{-2}. Figure 4 illustrates the excellent agreement between the numerical results of the in-house simulation and experimental data from You et al. [28]. The model demonstrated an average relative error of 1.6% when calculating the voltage, which is comparable to the level of agreement between the numerical simulations and experiments described in You et al. [28]. The relative error has been calculated by means of the following expression:

$$\text{Relative error (\%)} = \left(\frac{\text{Numerical model value} - \text{Experimental value}}{\text{Experimental value}} \right) \times 100 \quad (33)$$
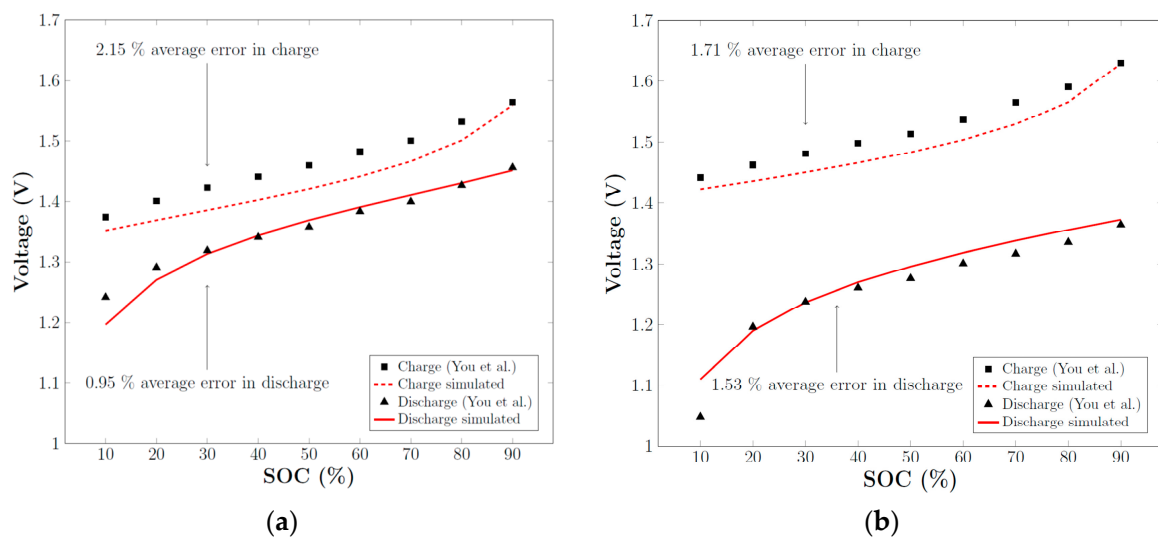

Figure 4. Comparison of experimentally obtained charge-discharge curves from [42] and simulated curves in a 5 cm^2 cell for: (**a**) a current density of 40 mA cm^{-2}; (**b**) a current density of 80 mA cm^{-2}.

3.2. Artificial Neural Network Validation

To evaluate the accuracy of the ANN predictions, the correlation coefficient (R-value) of the test set is considered, since these cases are unknown for the network, and therefore determine the generalisability of the proposed networks. The R-values after training ANN1 and ANN2 are shown in Figure 5.

The R-values for ANN1 and ANN2 were 0.99927 and 0.99516. Both models provide relatively high correlation coefficients, indicating a high level of confidence in ANN prediction. It should be noted that the two graphs do not have the same vertical scale and that ANN1 has no outliers, whereas the more complex ANN2 has a substantial set of outliers at the extremes.

To further analyse the performance of the two neural networks, Figure 6 shows a comparison between the predictions of ANN1 for both charging and discharging, together with the CFD results for the considered cases. The ANN1 prediction is illustrated as a surface, and the CFD results are illustrated using black markers. The possibility of spanning a continuous and smooth surface between CFD cases enables the prediction of a well-formulated ANN to have few outliers, which is the case for the ANN1 model.
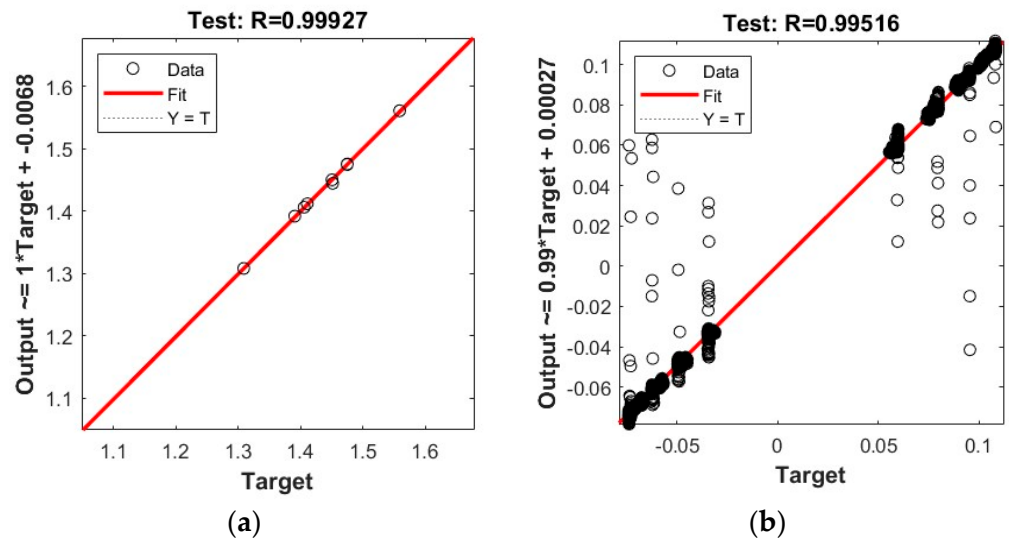
Figure 5. Correlation coefficient of the test set ANN for overpotential prediction: (**a**) ANN1 for voltage prediction; (**b**) ANN2 for overpotential prediction.
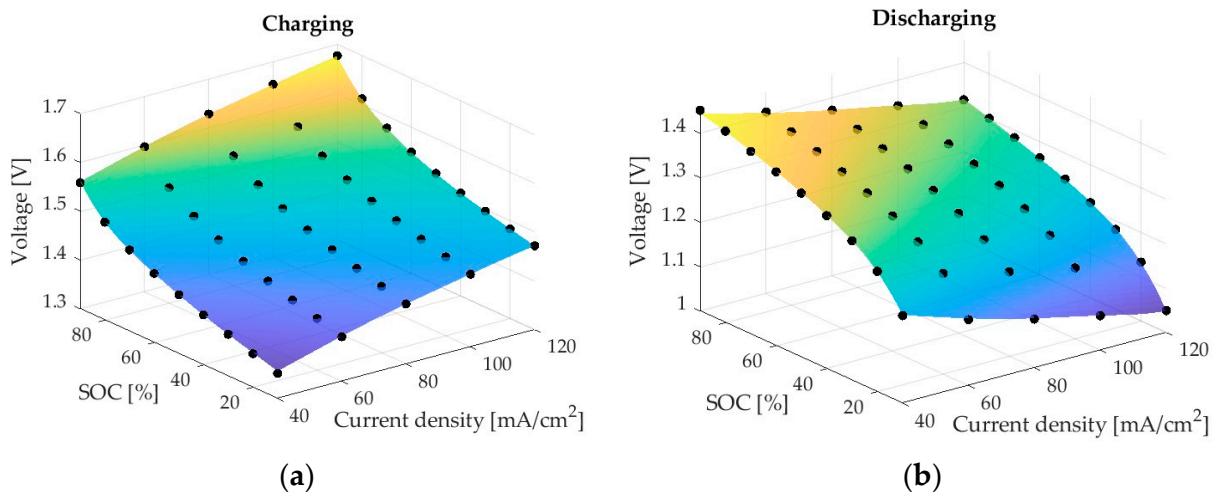

Figure 6. ANN1 predictions of voltage (coloured surfaces) and CFD results (black circles): (**a**) charging; (**b**) discharging.

As previously mentioned, ANN2, compared to ANN1, is modelling a more complex phenomenon and has a non-negligible set of outliers of correlation coefficients. The intricate modelling is illustrated by detailed studies of the overpotential for a current density of 60 mA/cm^2 in the discharge mode for an SoC of 50%. Figure 7 shows a section view across the membrane (the xy plane in Figure 1), where the positive and negative electrode voltages across the membrane and neighbouring fluid are shown for the numerical simulations to the left and ANN2 to the centre. Observing the numerical results, one may note a near-discrete step in the electrode voltage over the membrane and a non-uniform distribution, particularly near the lower boundary. ANN2 captured a substantial fraction of the electrode voltage distribution of the section cut, as can be observed by comparing the results with the CFD results. However, there were clear discrepancies near the membrane and the lower boundary. These discrepancies are emphasised by the subtraction of the numerical results and ANN2, as illustrated on the rightmost surface in Figure 7.
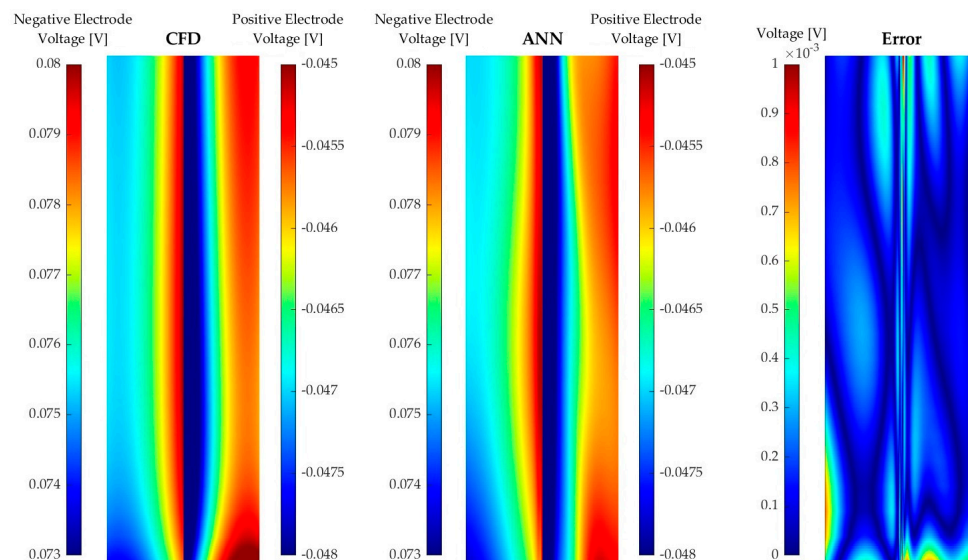
Figure 7. Comparison between the CFD data and ANN predictions of the overpotential for a current density of 60 mA/m^2 in discharge mode for a State of Charge of 50%.

3.3. ANN Effiency Benchmark

Table 6 summarises the computational times required for the CFD calculation, ANN1, and ANN2 for a workstation with a single Intel Xeon Gold 5120 CPU. The effectiveness of the ANN was benchmarked based on the time required to conduct a single CFD simulation.

Table 6. Computational time required for each method.

Method	Computational Time	Speed Up
CFD	50 s	-
ANN1 (Voltage)	0.0032 s	15,625
ANN2 (Overpotential)	0.1875 s	266.7

The results demonstrate that ANNs can significantly reduce the computational time required to obtain the results. ANN1 achieved a speed-up of 15,625 times the CFD, whereas with ANN2 for overpotential prediction, a speed-up of 266.7 was obtained.

4. Conclusions

This study investigated the predictive capabilities of Artificial Neural Networks (ANNs) for cell voltage and overpotential in Vanadium Redox Flow (VRF) cells. Two ANN models were developed, one for cell voltage and another for overpotential, and trained on a dataset generated by a two-dimensional numerical CFD model based on previous research by Shah et al. [30] and Knehr et al. [31]. The accuracy of the CFD models was verified with experimental results from You et al. [28], with an average discrepancy of 1.6% for the charge and discharge curves at two different current densities (40 and 80 mA cm^{-2}).

The results demonstrate that the ANN models are capable of accurately predicting a wide range of State of Charge and current density conditions with high precision during both charge and discharge. Additionally, the ANN model showed high confidence in overpotential predictions for most of the domains, with only minor performance deterioration in the high-gradient region over the membrane and selected boundaries of the simulated domain.

The computational power required for the ANN models was significantly less than that required for the CFD simulations, reducing the required computational power by up to four orders of magnitude. This reduction in power, combined with high confidence in the predictions, provides a promising option for rapid evaluation and system integration

for optimisation. The most compelling application may be the integration of ANN models on hardware for on-site monitoring and real-time cell prediction.

Author Contributions: Conceptualization, J.M.-L. and U.F.-G.; methodology, K.P.-P.; software, E.S.-D.; validation, J.M.-L. and U.F.-G.; formal analysis, J.O.; investigation, U.F.-G.; resources, E.S.-D.; data curation, K.P.-P. and I.J.; writing—review and editing, J.M.-L., K.P.-P., U.F.-G. and I.J.; visualization, J.O.; supervision, E.S.-D.; project administration, U.F.-G.; funding acquisition, U.F.-G. All authors have read and agreed to the published version of the manuscript.

Data Availability Statement: All data generated in the current study are available upon reasonable request to the corresponding author.

Conflicts of Interest: Authors Eduardo Sánchez-Díez and Javier Olarte are employed by the Centre for Cooperative Research on Alternative Energies (CIC EnergiGUNE). The remaining authors declare that the research was conducted in the absence of any commercial or financial relationships that could be construed as a potential conflict of interest.

Nomenclature

a	Specific surface area [m^2]
c	Concentration [$mol\ m^{-3}$]
D	Diffusion coefficient
d_f	Fiber diameter [m]
E	Equilibrium potential [V]
F	Faraday constant [$C\ mol^{-1}$]
h	Length [m]
h_i	Postsynaptical output (ANN)
i	Current density [$mA\ cm^{-2}$]
i_0	Exchange current density
i_R	Electrochemical reaction rate
K	Permeability [m^2]
K_{ck}	Kozeny-Carman constant
k	Reaction rate constant [$m\ s^{-1}$]
L	Thickness [m]
N	Charged species flux [$mol\ m^{-3}\ s^{-1}$]
p	Pressure [Pa]
Q	Volumetric flow rate [$ml\ min^{-1}$]
R	Ideal gas constant [$J\ mol^{-1}\ K^{-1}$]
S	Source term [$mol\ m^{-3}\ s^{-1}$]
T	Temperature [K]
t	Time
u	Mobility [$mol\ s\ kg^{-1}$]
u	Velocity [$m\ s^{-1}$]
w	Width [m]
x	Input (ANN)
y	Output (ANN)
z	Species charge

Greek	
α	Charge transfer coefficient
ε	Porosity
η	Overpotential [V]
σ	Conductivity [S m^{-1}]
φ	Potential [V]
μ	Dynamic viscosity [Pa s]
θ	Layer bias (ANN)
ω	Layer weights (ANN)

Superscripts and subscripts	
+	Positive side or cathode
−	Negative side or anode
'	Standard
avg	Average
e	Electrode
eff	Effective
i	Species
in	Inlet
l	Liquid
m	Membrane
out	Outlet
s	Solid

Abbreviations	
ANN	Artificial Neural Network
CFD	Computational Fluid Dynamics
MLP-BP	Multi-Layer Perceptron with Backpropagation
RFB	Redox Flow Battery
VRFB	Vanadium Redox Flow Battery

References

1. Sayed, E.T.; Olabi, A.G.; Alami, A.H.; Radwan, A.; Mdallal, A.; Rezk, A.; Abdelkareem, M.A. Renewable Energy and Energy Storage Systems. *Energies* **2023**, *16*, 1415. [CrossRef]
2. Mitali, J.; Dhinakaran, S.; Mohamad, A.A. Energy Storage Systems: A Review. *Energy Storage Sav.* **2022**, *1*, 166–216. [CrossRef]
3. Sánchez-Díez, E.; Ventosa, E.; Guarnieri, M.; Trovò, A.; Flox, C.; Marcilla, R.; Soavi, F.; Mazur, P.; Aranzabe, E.; Ferret, R. Redox Flow Batteries: Status and Perspective towards Sustainable Stationary Energy Storage. *J. Power Sources* **2021**, *481*, 228804. [CrossRef]
4. Arévalo-Cid, P.; Dias, P.; Mendes, A.; Azevedo, J. Redox Flow Batteries: A New Frontier on Energy Storage. *Sustain. Energy Fuels* **2021**, *5*, 5366–5419. [CrossRef]
5. Skyllas-Kazacos, M.; Menictas, C.; Lim, T. Redox Flow Batteries for Medium- to Large-Scale Energy Storage. In *Electricity Transmission, Distribution and Storage Systems*; Melhem, Z., Ed.; Woodhead Publishing Series in Energy; Woodhead Publishing: Sawston, UK, 2013; pp. 398–441, ISBN 978-1-84569-784-6.
6. Olabi, A.G.; Allam, M.A.; Abdelkareem, M.A.; Deepa, T.D.; Alami, A.H.; Abbas, Q.; Alkhalidi, A.; Sayed, E.T. Redox Flow Batteries: Recent Development in Main Components, Emerging Technologies, Diagnostic Techniques, Large-Scale Applications, and Challenges and Barriers. *Batteries* **2023**, *9*, 409. [CrossRef]
7. Lourenssen, K.; Williams, J.; Ahmadpour, F.; Clemmer, R.; Tasnim, S. Vanadium Redox Flow Batteries: A Comprehensive Review. *J. Energy Storage* **2019**, *25*, 100844. [CrossRef]
8. Weber, A.Z.; Mench, M.M.; Meyers, J.P.; Ross, P.N.; Gostick, J.T.; Liu, Q. Redox Flow Batteries: A Review. *J. Appl. Electrochem.* **2011**, *41*, 1137–1164. [CrossRef]
9. Alotto, P.; Guarnieri, M.; Moro, F. Redox Flow Batteries for the Storage of Renewable Energy: A Review. *Renew. Sustain. Energy Rev.* **2014**, *29*, 325–335. [CrossRef]
10. Cunha, Á.; Martins, J.; Rodrigues, N.; Brito, F.P. Vanadium Redox Flow Batteries: A Technology Review. *Int. J. Energy Res.* **2015**, *39*, 889–918. [CrossRef]
11. Skyllas-Kazacos, M.; Rychcik, M.; Robins, R.G.; Fane, A.G.; Green, M.A. New All-Vanadium Redox Flow Cell. *J. Electrochem. Soc.* **1986**, *133*, 1057. [CrossRef]
12. Esan, O.C.; Shi, X.; Pan, Z.; Huo, X.; An, L.; Zhao, T.S. Modeling and Simulation of Flow Batteries. *Adv. Energy Mater.* **2020**, *10*, 2000758. [CrossRef]
13. Aluko, A.; Knight, A. A Review on Vanadium Redox Flow Battery Storage Systems for Large-Scale Power Systems Application. *IEEE Access* **2023**, *11*, 13773–13793. [CrossRef]

14. Chen, R.; Kim, S.; Chang, Z. *Redox Flow Batteries: Fundamentals and Applications*; CRC Press: Boca Raton, FL, USA, 2017; pp. 103–118, ISBN 978-953-51-5421-1.

15. Lucas, A.; Chondrogiannis, S. Smart Grid Energy Storage Controller for Frequency Regulation and Peak Shaving, Using a Vanadium Redox Flow Battery. *Int. J. Electr. Power Energy Syst.* **2016**, *80*, 26–36. [CrossRef]

16. Arribas, B.; Melicio, R.; Ginja Teixeira, J.; Mendes, V.M.F. Vanadium Redox Flow Battery Storage System Linked to the Electric Grid. *Renew. Energy Power Qual. J.* **2016**, *1*, 1025–1030. [CrossRef]

17. Sun, C.; Negro, E.; Vezzù, K.; Pagot, G.; Cavinato, G.; Nale, A.; Herve Bang, Y.; Di Noto, V. Hybrid Inorganic-Organic Proton-Conducting Membranes Based on SPEEK Doped with WO3 Nanoparticles for Application in Vanadium Redox Flow Batteries. *Electrochim. Acta* **2019**, *309*, 311–325. [CrossRef]

18. Choi, C.; Kim, S.; Kim, R.; Choi, Y.; Kim, S.; Jung, H.; Yang, J.H.; Kim, H.-T. A Review of Vanadium Electrolytes for Vanadium Redox Flow Batteries. *Renew. Sustain. Energy Rev.* **2017**, *69*, 263–274. [CrossRef]

19. Yu, F.; Zhao, W.; Leung, P.; Mohamed, M.R.; Wei, L.; Shah, A.; Liao, Q. Performance Evaluation of a Scaled-Up Membraneless Organic-Based Hybrid Flow Battery. *Batteries* **2023**, *9*, 336. [CrossRef]

20. Liu, Y.; Goulet, M.-A.; Tong, L.; Liu, Y.; Ji, Y.; Wu, L.; Gordon, R.G.; Aziz, M.J.; Yang, Z.; Xu, T. A Long-Lifetime All-Organic Aqueous Flow Battery Utilizing TMAP-TEMPO Radical. *Chem* **2019**, *5*, 1861–1870. [CrossRef]

21. Winsberg, J.; Hagemann, T.; Janoschka, T.; Hager, M.D.; Schubert, U.S. Redox-Flow Batteries: From Metals to Organic Redox-Active Materials. *Angew. Chem. Int. Ed.* **2017**, *56*, 686–711. [CrossRef]

22. Tas, M.; Elden, G. A Comprehensive Review of Carbon- and Metal-based Electrocatalysts in the Vanadium Redox Flow Battery. *Energy Storage* **2021**, *4*, e265. [CrossRef]

23. Pugach, M.; Kondratenko, M.; Briola, S.; Bischi, A. Zero Dimensional Dynamic Model of Vanadium Redox Flow Battery Cell Incorporating All Modes of Vanadium Ions Crossover. *Appl. Energy* **2018**, *226*, 560–569. [CrossRef]

24. König, S.; Suriyah, M.R.; Leibfried, T. Validating and Improving a Zero-Dimensional Stack Voltage Model of the Vanadium Redox Flow Battery. *J. Power Sources* **2018**, *378*, 10–18. [CrossRef]

25. Chen, Y.; Xu, Z.; Wang, C.; Bao, J.; Koeppel, B.; Yan, L.; Gao, P.; Wang, W. Analytical Modeling for Redox Flow Battery Design. *J. Power Sources* **2021**, *482*, 228817. [CrossRef]

26. Yin, C.; Gao, Y.; Guo, S.; Tang, H. A Coupled Three Dimensional Model of Vanadium Redox Flow Battery for Flow Field Designs. *Energy* **2014**, *74*, 886–895. [CrossRef]

27. Ma, X.; Zhang, H.; Xing, F. A Three-Dimensional Model for Negative Half Cell of the Vanadium Redox Flow Battery. *Electrochim. Acta* **2011**, *58*, 238–246. [CrossRef]

28. Wang, Y.; Cho, S.C. Analysis and Three-Dimensional Modeling of Vanadium Flow Batteries. *J. Electrochem. Soc.* **2014**, *161*, A1200–A1212. [CrossRef]

29. Xu, Q.; Zhao, T.S.; Leung, P.K. Numerical Investigations of Flow Field Designs for Vanadium Redox Flow Batteries. *Appl. Energy* **2013**, *105*, 47–56. [CrossRef]

30. Wang, Q.; Qu, Z.G.; Jiang, Z.Y.; Yang, W.W. Numerical Study on Vanadium Redox Flow Battery Performance with Non-Uniformly Compressed Electrode and Serpentine Flow Field. *Appl. Energy* **2018**, *220*, 106–116. [CrossRef]

31. Sun, J.; Zheng, M.; Luo, Y.; Yu, Z. Three-Dimensional Detached Serpentine Flow Field Design for Redox Flow Batteries. *J. Power Sources* **2019**, *428*, 136–145. [CrossRef]

32. Portal-Porras, K.; Fernandez-Gamiz, U.; Zulueta, E.; Garcia-Fernandez, R.; Etxebarria Berrizbeitia, S. Active Flow Control on Airfoils by Reinforcement Learning. *Ocean Eng.* **2023**, *287*, 115775. [CrossRef]

33. Portal-Porras, K.; Fernandez-Gamiz, U.; Zulueta, E.; Ballesteros-Coll, A.; Zulueta, A. CNN-Based Flow Control Device Modelling on Aerodynamic Airfoils. *Sci. Rep.* **2022**, *12*, 8205. [CrossRef] [PubMed]

34. Jacob, S.J.; Mrosek, M.; Othmer, C.; Köstler, H. Deep Learning for Real-Time Aerodynamic Evaluations of Arbitrary Vehicle Shapes. *SAE Int. J. Passeng. Veh. Syst.* **2022**, *15*, 77–90. [CrossRef]

35. Portal-Porras, K.; Fernandez-Gamiz, U.; Zulueta, E.; Garcia-Fernandez, R.; Irigaray, O. Parametric Study of Vortex Generators on a Fin-and-Tube Heat Exchanger. *Energy Sources Part A Recovery Util. Environ. Eff.* **2023**, *45*, 10051–10072. [CrossRef]

36. Ugarte-Anero, A.; Fernandez-Gamiz, U.; Portal-Porras, K.; Zulueta, E.; Urbina-Garcia, O. Computational Characterization of the Behavior of a Saliva Droplet in a Social Environment. *Sci. Rep.* **2022**, *12*, 6405. [CrossRef] [PubMed]

37. Che, X.; Tang, W.; Dong, J.; Aili, D.; Yang, J. Anion Exchange Membranes Based on Long Side-Chain Quaternary Ammonium-Functionalized Poly(Arylene Piperidinium)s for Vanadium Redox Flow Batteries. *Sci. China Mater.* **2022**, *65*, 683–694. [CrossRef]

38. Shah, A.A.; Watt-Smith, M.J.; Walsh, F.C. A Dynamic Performance Model for Redox-Flow Batteries Involving Soluble Species. *Electrochim. Acta* **2008**, *53*, 8087–8100. [CrossRef]

39. Knehr, K.; Agar, E.; Dennison, C.; Kalidindi, A.; Kumbur, E. A Transient Vanadium Flow Battery Model Incorporating Vanadium Crossover and Water Transport through the Membrane. *J. Electrochem. Soc.* **2012**, *159*, A1446–A1459. [CrossRef]

40. Yamamura, T.; Watanabe, N.; Yano, T.; Shiokawa, Y. Electron-Transfer Kinetics of Np^{3+}/Np^{4+}, NpO_2^{+}/NpO_2^{2+}, V^{2+}/V^{3+}, and VO^{2+}/VO_2^{+} at Carbon Electrodes. *J. Electrochem. Soc.* **2005**, *152*, A830. [CrossRef]

41. Newman, J.; Thomas-Alyea, K.E. *Electrochemical Systems*; John Wiley & Sons: Hoboken, NJ, USA, 2004; ISBN 978-0-471-47756-3.

42. You, D.; Zhang, H.; Chen, J. A Simple Model for the Vanadium Redox Battery. *Electrochim. Acta* **2009**, *54*, 6827–6836. [CrossRef]

43. Zhou, H.; Zhang, H.; Zhao, P.; Yi, B. A Comparative Study of Carbon Felt and Activated Carbon Based Electrodes for Sodium Polysulfide/Bromine Redox Flow Battery. *Electrochim. Acta* **2006**, *51*, 6304–6312. [CrossRef]

44. Sum, E.; Skyllas-Kazacos, M. A Study of the V(II)/V(III) Redox Couple for Redox Flow Cell Applications. *J. Power Sources* **1985**, *15*, 179–190. [CrossRef]
45. MATLAB—MathWorks. Available online: https://www.mathworks.com/products/matlab.html (accessed on 22 May 2023).
46. Deep Learning Toolbox. Available online: https://www.mathworks.com/products/deep-learning.html (accessed on 22 May 2023).